JOURNAL OF SPACECRAFT AND ROCKETS
Vol. 43, No. 5, September–October 2006

Afterbody Aeroheating Flight Data for Planetary Probe Thermal Protection System Design

Michael J. Wright and Frank S. Milos
NASA Ames Research Center, Moffett Field, California 95050
and
Philippe Tran
EADS SPACE Transportation, 78133 Les Mureaux Cedex, France

Nomenclature

D	=	body diameter
h	=	altitude
Kn	=	Knudsen number
L	=	body length
L/D	=	lift to drag ratio
ℓ	=	running length
M	=	Mach number
q	=	heat transfer rate
R	=	radius
Re	=	Reynolds number
r	=	radial distance from nose
s	=	path-length distance from stagnation point
t	=	time
u, V	=	velocity
x	=	axial distance
α	=	angle of attack, deg
γ	=	flight-path angle, deg
θ, ϕ	=	circumferential angle, deg
λ	=	mean free path
μ	=	viscosity
ρ	=	fluid density

Subscripts

aft	=	afterbody
b	=	base
c	=	corner
D	=	diameter
e	=	edge
exp	=	experimental

Michael Wright is a Senior Research Scientist at the NASA Ames Research Center in the Reacting Flow Environments Branch, specializing in computational aerothermodynamics for Earth- and planetary-entry vehicles. He is the developer of the DPLR hypersonic computational fluid dynamics code, which is the primary aerothermodynamic analysis tool at Ames. He has authored or coauthored more than 50 papers in the field and is the two-time recipient of the AIAA Best Thermophysics Paper Award (2001 and 2004). He received his Ph.D. in aerospace engineering from the University of Minnesota in 1997 and is a Senior Member of AIAA.

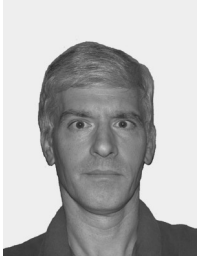

Frank Milos is a Senior Research Scientist in the Thermal Protection Materials and Systems Branch at NASA Ames Research Center, specializing in computational modeling and analysis of both reusable and ablative TPS for Earth- and planetary-entry vehicles. He is coinventor of the thermal protection system (TPS) analysis codes FIAT and TITAN and the materials database program TPSX. He was principal investigator for the heat-shield data from the Jupiter Galileo and Mars Pathfinder probes and has performed analysis of TPS for numerous NASA vehicles including Stardust, X-34, and X-37. He received his Ph.D. in chemical engineering from Stanford University in 1986 and is a Senior Member of AIAA. He has authored or coauthored more than 65 conference and journal papers.

Philippe Tran graduated from Ecole Nationale Supérieure de Mécanique et d'Aérotechnique Poitiers and joined EADS SPACE Transportation (formerly Aérospatiale) Les Mureaux in 1985 as an aerothermal engineer. He has developed boundary-layer codes and has been in charge of engineering methods in the fluid mechanics department. He has been in charge of aerothermodynamics studies of Earth or planetary entry vehicles including the Hermès Space Plane, the Atmospheric Reentry Demonstrator, X-38, and the Huygens probe. He was the system engineer for Mars entry descent and landing system studies in 2003–2004. He is now in charge of aerodynamics and aerothermodynamics studies of all civilian entry vehicles in the reentry systems and technologies department at EADS SPACE Transportation.

Received 16 May 2005; presented as Paper 2005-4815 at the AIAA 38th Thermophysics Conference, Toronto, ON, Canada, 6–9 June 2005; revision received 24 August 2005; accepted for publication 24 August 2005.

GLL = gradient-length local [Eq. (1)]
k = roughness height
max = maximum
n = nose
o = initial or entry
stag = stagnation
tot = total
tr = transition
∞ = freestream
θ = momentum thickness

I. Introduction

UNCERTAINTY levels associated with aeroheating predictions for the design of the afterbody of planetary probes are typically assumed to be in the range of 50–300%. This level can have a significant effect on thermal protection system (TPS) material selection and total mass. This conservatism in the afterbody heat-shield design will also shift the center of gravity aftward, which reduces the static stability of the probe and in some circumstances may necessitate the addition of ballast in the nose. Current design practice for an afterbody heat shield assumes a laminar, fully catalytic, nonablating surface. The predictions thus obtained are then augmented by a large factor of safety to account for such factors as turbulent transition, material response, and uncertainties in the baseline computations. In comparison, uncertainty levels for forebody convective heating predictions are typically about 15% for laminar flows and 30% for turbulent flows, up to a full order of magnitude smaller than those on the afterbody. A primary reason for the large uncertainty in afterbody heating predictions is a perceived sparsity of relevant data for validation of the computational tools. Ground test data are usually complicated by sting interference effects, although a limited amount of shock tunnel[1,2] and ballistic range[3] data exist. Some flight data at appropriate velocities are available, but many of the most relevant flights occurred in the 1960s, and for the most part these data have not been critically evaluated or used for code-validation purposes in more than 30 years. Recent attempts to propose dedicated flight experiments have failed to reach fruition. Therefore, it is important to thoroughly understand the limited flight data that are available to improve the design fidelity of the next generation of Earth- and planetary-entry vehicles and to assess the need for additional focused flight testing.

This paper first reviews the physical modeling of a separated afterbody flow. Following this, we survey the available flight data for validating afterbody heating predictions and review prior computational analyses of these data, if any. In compiling flight data sources we use only those that are available in the open literature. Also, with few exceptions, we include only flights that achieved orbital-entry velocity or higher; sounding rocket flights and other similar data sources are not included because the aerothermal environment experienced during such flights is not representative of that encountered during actual planetary-entry missions. Also excluded are data from mid and high L/D ratio vehicles, such as the Shuttle Orbiter, which again are not representative of typical planetary probes. Finally, we provide recommendations for areas of further work and possible additional data or analysis that would aid in further reducing the afterbody aeroheating design uncertainty.

II. Flow Regimes and Physical Models

The principal features of a typical afterbody flow are illustrated in Fig. 1, which shows temperature contours overlaid with streamlines in the symmetry plane of an Apollo entry vehicle at 18-deg angle of attack. Although the details of the flow vary with geometry and freestream conditions, the general features remain the same. The forebody flowfield is dominated by a strong bow shock wave. As the flow turns around the shoulder of the capsule it rapidly expands and can separate. For the case shown in Fig. 1 the leeward side flow separates just after the shoulder, whereas the windward side flow remains attached until the rear apex. A shear layer separates the outer flow from the recirculating inner core, which consists of multiple counterrotating vortices. The separated flow region is called the near

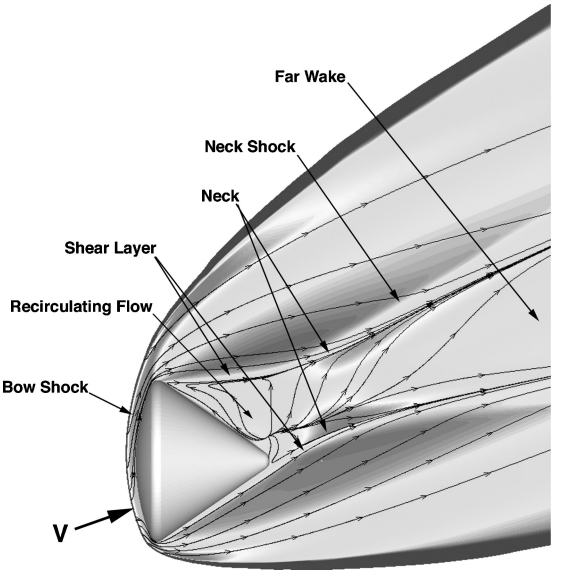

Fig. 1 Temperature contours and streamlines in the symmetry plane of Apollo AS-202, showing major afterbody flowfield features (V = 7.80 km/s, h = 66 km, α = 17.8 deg).

wake. The separation shear layer eventually coalesces, creating the "neck," or narrowest point in the wake. A shock forms at this point, called the neck or wake shock, which compresses the flow, leading to local maxima in temperature and pressure. Beyond the neck is the far wake, which extends for many body diameters downstream as the momentum deficit created by the passing capsule is slowly recovered. In a hypersonic flow the wake is oriented parallel to the freestream velocity vector, as seen in Fig. 1.

During entry, a planetary probe will pass from a free molecular (collisionless) to a noncontinuum and finally to a continuum flow regime. The transition between these regimes is determined by evaluation of the freestream Knudsen number, given by $Kn_\infty = \lambda_\infty / D$. Free molecular flow is usually defined as the region where $Kn_\infty > 100$, whereas continuum flow is usually defined as the region where $Kn_\infty < 0.03$ (Ref. 4). However, this criterion is not appropriate for separated base flows, because the local mean free path in the separation region can be much larger than that in the freestream. A more useful determination can be made by using the density ρ gradient length local Knudsen number proposed by Boyd et al.,[5] given by

$$Kn_{\mathrm{GLL}} = \frac{\lambda}{\rho}\left|\frac{d\rho}{dl}\right|_{\max} \tag{1}$$

where λ and ρ are local values and the derivative is evaluated along the maximum gradient direction. Following the work of Boyd et al.,[5] we assume that continuum breakdown occurs when $Kn_{\mathrm{GLL}} > 0.1$. This criterion results in a more useful determination of continuum breakdown in a separated flow, because although the local mean free path in the separation region can be quite large, the density gradient is usually small, which delays the onset of noncontinuum effects. For afterbody flows the highest values of Kn_{GLL} are typically observed near the flow separation point because of large density gradients. Although Boyd et al.[5] do not quantify the effect of continuum breakdown on computational fluid dynamics (CFD) predictions of heat transfer, it has been shown[6] that continuum simulations, in general, will overpredict heating in regions of noncontinuum flow. Numerical solutions for free molecular and noncontinuum flows are typically obtained using a direct simulation Monte Carlo (DSMC) methodology. An excellent review on the status of DSMC calculations for noncontinuum wake flows was presented by Moss and Price.[7] However, for many problems of interest the majority of the aeroheating occurs in continuum flow, where Navier–Stokes–based CFD methods are applicable.

When a probe enters a planetary atmosphere at high velocity, the resulting shock wave will thermally excite, dissociate, and possibly

ionize the gas. To accurately model the resulting flowfield, including the wake of the probe, a nonequilibrium model is usually required.[8] Each chemical and thermal relaxation process has an associated characteristic time, and the rapid expansion of the flow into the wake will decrease the collision rate, which freezes the slower processes (such as vibrational relaxation) while the faster chemical relaxation processes continue at a finite rate. The details of the base flow structure and resulting heating rates can be very sensitive to the resulting nonequilibrium state of the gas.[9–11] In addition, each planetary atmosphere is unique, and the details of the atmospheric constituents and their gas-phase reactions in the shock layer have a large influence on the resulting wake flow. An excellent review of the thermodynamic and chemical–kinetic models employed for CFD simulations of a nonequilibrium flowfield is given by Gnoffo et al.[12]

The afterbody flowfield will likely transition from a laminar to a turbulent flow during the entry. In a separated base flow, wake transition begins in the far wake and travels upstream with increasing freestream Re until reaching the neck, where it is (temporarily) stopped by the adverse pressure gradient. In the near-wake (base) region transition begins in the separation shear layer. Lees[13] and Zeiberg[14] give a transition correlation for the free shear layer in a two-dimensional or axisymmetric flow that is based on a local transition Reynolds number, defined as

$$Re_{\mathrm{tr}} = \rho_e u_e \ell / \mu_e \tag{2}$$

where ℓ is the running length of the shear layer from the separation point, and the local density, velocity, and viscosity are evaluated based on fluid properties at the outer edge of the shear layer. The critical transition Reynolds number is a function of the edge Mach number and ranges from about 2×10^4 at $M_e = 2$ to about 5×10^6 at $M_e = 5$. This criterion is based on free-flight data but does not include effects of upstream ablation product gas injection, which can destabilize the boundary layer and could also affect the shear layer and separated flow region. Transition criteria for the attached portions of the afterbody flow are analogous to those used on the forebody, including $Re_\theta / M_e \sim$ const. for smooth body transition[15] or roughness height–based local Reynolds number criteria ($Re_{kk} \sim$ const.) for rough ablating surfaces.[16] Injection of ablation products into the upstream boundary layer can also promote turbulent transition in a separated flow.[17] A recent paper by Schneider[18] reviews available ground test and flight data for turbulent transition on planetary-entry capsules, including afterbodies.

Low-Reynolds-number wake flows are steady with a structure dominated by a small number of large vortices. As the freestream Reynolds number increases, the extent of separation increases as well, and the vortex structure becomes more complex, with small counterrotating secondary and tertiary vortices. Eventually these vortices begin to oscillate and the base flow becomes unsteady. Moreover, the unsteadiness modes will be three dimensional, even for a nominally axisymmetric flowfield. Typically, the Reynolds number at which the flowfield becomes unsteady is near that at which transition to turbulence is predicted to begin. For many cases of interest, both events occur after the peak heating point on the trajectory. For these cases much of the heat pulse can be simulated assuming a continuum, laminar, steady flow.

Finally, wake flows are sensitive to the details of the volume grid used in the CFD analysis. Therefore it is important to generate a grid that is well aligned to anticipated flow features. In particular, it is important that the grid have sufficient points in the shoulder region to capture the rapid expansion and accurately predict the flow separation point and the angle of the resulting shear layer.[19] There must also be sufficient points in the separated flow region to resolve the relevant length scales that define the vortical structure and the wake compression, or neck. At higher Reynolds numbers the wake will consist of multiple counterrotating vortices that must be resolved. Care must also be taken to ensure that the grid completely encloses the subsonic portion of the wake, which can extend several body diameters downstream.

III. Available Flight Data and Previous Validation Attempts

Much of the most relevant flight data for validation of afterbody aeroheating predictions were obtained during the Apollo program, although there are also limited data from other American and European entry probes. This section summarizes the available flight data and discusses published attempts at postflight analysis, if any. All American and European flights with available afterbody flight data meeting the criteria discussed in the introduction are summarized in Table 1. In Table 1, the column labeled "Geometry" is a brief description of the forebody configuration of the entry vehicle, "Destination" is the planet where the spacecraft entered, V is the atmosphere-relative entry velocity, α is the angle of attack, and γ is the relative entry flight-path angle. The column labeled "Utility" is a subjective measure of the suitability of the flight data for code validation. The reasons for the assigned utility is discussed for each flight in the following sections. Finally, the column labeled "Recent analysis" indicates whether any attempt has been made within the past 20 years to compare high-fidelity computational predictions with the flight data obtained. Any such comparisons are briefly reviewed in the following sections. It is likely that Russian (Soviet) flight data also exist, although no references to any such data were located in the open literature.

A. Mercury Program

The Mercury program began with four Redstone-launched suborbital flights. These four missions included the first American in space, Alan Shepherd, aboard Freedom 7 in May 1961. No afterbody flight data from the Mercury-Redstone flights have been located at this time. In addition, a series of sounding rocket–launched Little-Joe and Mercury-Scout test vehicles were flown during the program. Some of these test flights carried afterbody instrumentation,[20] but these were all low-velocity flights and thus are not included in this review.

Early in the program it was realized that an ablative forebody heat shield would be preferable to a metallic heat sink to survive the increased heat fluxes and loads of orbital (vs suborbital) reentry. Therefore, a flight test of a Mercury prototype capsule with a fiberglass-phenolic ablative heatshield was flown in September 1959, in part to prove the viability of this concept.[21] This flight test vehicle, nicknamed Big-Joe, was heavily instrumented with 52 thermocouples (TCs) and 13 ablation char-rate sensors in the forebody heatshield and another 52 TCs and 2 pressure sensors on the afterbody.[22] In addition, the interior of the afterbody was coated with a temperature-sensitive paint to provide some redundancy in measured peak afterbody temperatures. Figure 2 shows a schematic of the Big-Joe test vehicle. Exact instrumentation locations are given in Ref. 23. The conical pressure vessel portion of the afterbody was constructed of smooth Inconel (a nickel-based alloy) sheets, and the remainder of the afterbody surface was constructed of corrugated

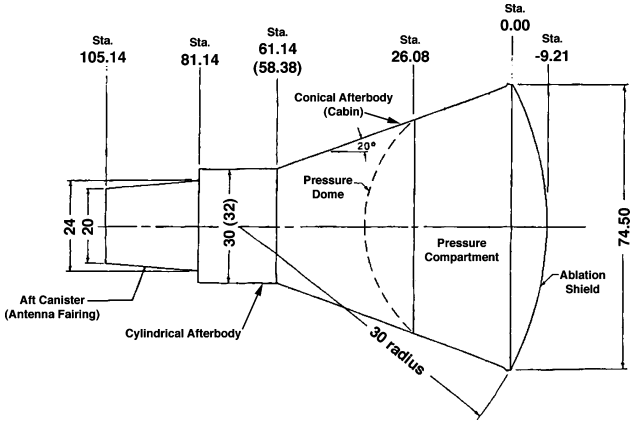

Fig. 2 Schematic of the Big-Joe and Mercury capsule reentry configuration (adapted from Refs. 23 and 25). All dimensions in inches. Where dimensions or names differ, those for Mercury are given in parentheses under those for Big-Joe.

Table 1 Summary of entry flights with usable afterbody aeroheating data

Flight	Entry date	Geometry	Destination	V, km/s	α, deg	γ, deg	Utility	Recent analysis?
Big-Joe	9 Sept. 1959	Truncated sphere	Earth	6.3	4	−0.9	Low	No
MA-2	21 Feb. 1961	Truncated sphere	Earth	5.5	13		Med.	No
MA-5	29 Nov. 1961	Truncated sphere	Earth	7.4	0	−1	Med.	No
MA-7	24 May 1962	Truncated sphere	Earth	7.4	0	−1	Med.	No
MA-8	3 Oct. 1962	Truncated sphere	Earth	7.4	0	−1	Med.	No
Fire-I	14 April 1964	Truncated sphere	Earth	11.5	0	−15	Low	No
GT-2	19 Jan. 1965	Truncated sphere	Earth	7.4	18	−3	Med.	No
GT-3	23 March 1965	Truncated sphere	Earth	7.4	10	−1	Med.	No
Fire-II	22 May 1965	Truncated sphere	Earth	11.3	0	−15	High	Yes
GT-4	3 June 1965	Truncated sphere	Earth	7.4	12	−1	Med.	No
AS-201	26 Feb. 1966	Truncated sphere	Earth	7.7	20	−9	High	No
AS-202	25 Aug. 1966	Truncated sphere	Earth	8.3	18	−3.5	High	Yes
Apollo 4	9 Nov. 1967	Truncated sphere	Earth	10.7	25	−7	High	No
Apollo 6	4 April 1968	Truncated sphere	Earth	9.6	25	−6	High	No
Reentry F	22 April 1968	5-deg slender cone	Earth	6	0	−20	High	No
Viking I	20 July 1976	70-deg sphere cone	Mars	4.5	11	−17	Med.	Yes
Viking II	3 Sept. 1976	70-deg sphere cone	Mars	4.5	11	−17	Med.	No
Galileo	7 Dec. 1995	45-deg sphere cone	Jupiter	47.4	0	−8.5	Low	Yes
Pathfinder	4 July 1997	70-deg sphere cone	Mars	7.5	0	−14	Med.	Yes
MIRKA	23 Oct. 1997	Flat-based sphere	Earth	7.6	0	−2.5	Low	No
ARD	12 Oct. 1998	Truncated sphere	Earth	7.5	21	−2.6	High	Yes

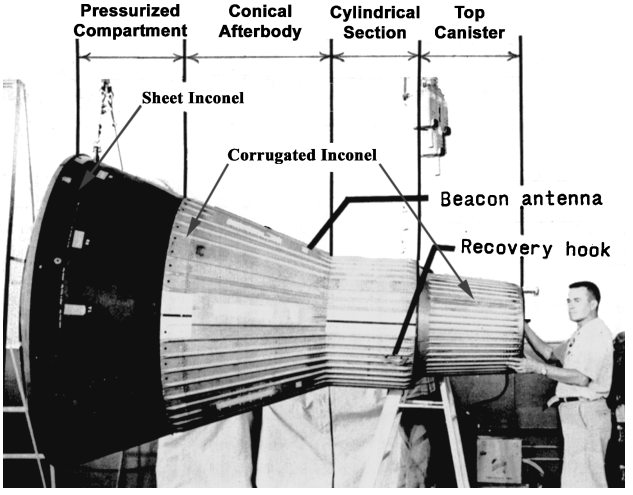

Fig. 3 Photograph of the Big-Joe Mercury test vehicle prior to launch (adapted from Ref. 23). Ablative forebody heatshield is on the left.

Fig. 4 Photograph of the Mercury MA-4 capsule being hoisted onto the recovery ship (courtesy of NASA image archives).

Inconel. (See Fig. 3 for a photograph of the flight vehicle.) The afterbody surface was corrugated primarily to provide increased shear strength during launch and ascent. Unfortunately, the Big-Joe flight was only partially successful. A stage-separation problem resulted in a failure to achieve the intended entry conditions. The delayed separation also caused the reaction-control system to remain on until the fuel was depleted.[24] The spacecraft then assumed an aerodynamically maintained trim angle of attack of about 5 deg because of an offset center of gravity (c.g.) but underwent large α oscillations caused by the lack of active control. Oscillations in α were about ± 15 deg near the peak heating point on the trajectory and as much as ± 25 deg early and late in the entry, with a frequency of about $\frac{1}{2}$ to 1 cycle per second.[23] This frequency was comparable to the sampling rate of the afterbody thermocouples (about 0.62 s per sample),[22] making it impossible to detect heating variations resulting from the α oscillations. A preliminary quick look at the data was presented in Ref. 22, and a more thorough data analysis was performed in Ref. 23. The heating rates to the afterbody were generally lower than predicted using modified flat-plate correlations. One notable exception to this trend was a localized region of high heating near the middle of the windward side of the cylindrical section. In this region a peak heat flux of 31.2 W/cm^2 was measured and a postflight inspection revealed that the Inconel was buckled from thermal damage. This hot spot was not predicted by theory nor was it seen in preflight wind-tunnel testing.[23] The reasons for this local hot spot were not known but were suspected to be shear-layer impingement and/or transition to turbulence.[23] However, given the large amplitude α oscillations, it is not clear why the effects of such an impingement would remain so localized on the cylindrical section.

Afterbody flight heating data are also published for four other Atlas-launched Mercury flights: Mercury-Atlas 2 (MA-2), which had 17 afterbody TCs, MA-5 with 9 TCs, MA-7 with 12 TCs, and MA-8 with 16 TCs.[25] Unfortunately, the MA-1 flight, which had afterbody heating measurements as a primary mission objective and was instrumented with 51 afterbody TCs,[21] exploded during launch in July 1960. Relevant entry conditions for the four successful test flights are given in Table 1. Figure 2 shows a schematic of the Mercury reentry configuration. Instrumentation locations for all four flight vehicles are given in Ref. 25. The major differences between the final Mercury-Atlas capsule and the Big-Joe test vehicle were the length of the cylindrical section and the afterbody TPS material, which was changed from Inconel to corrugated René 41 (a related nickel-based alloy) on the conical and aft sections.[25] Beryllium plates were used on the cylindrical section because of the high heating rates measured in this area during the Big-Joe test.[21] Figure 4 shows a photograph of the MA-4 spacecraft. Note that, in contrast

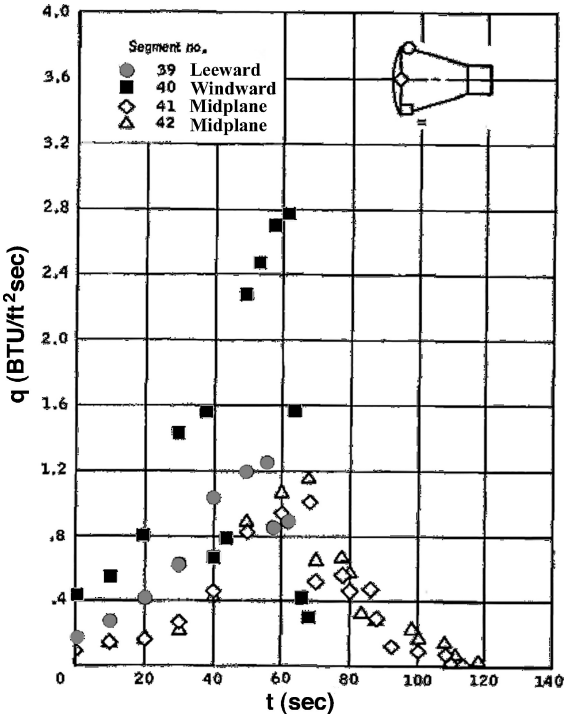

Fig. 5 Reentry heating data for the Mercury MA-2 capsule at four circumferential afterbody thermocouple locations (from Ref. 25).

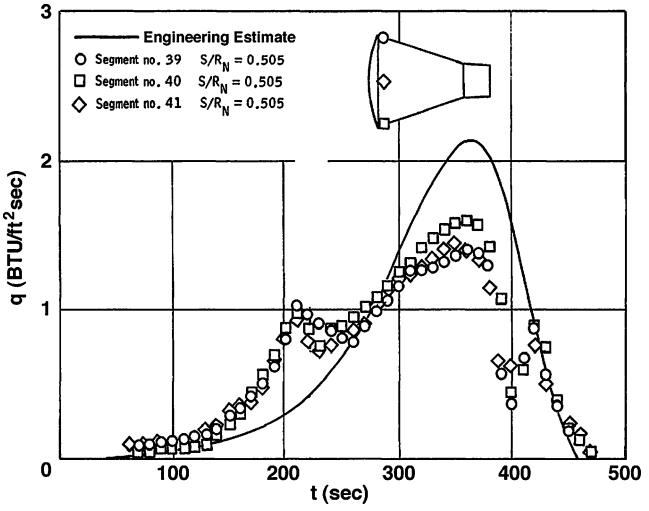

Fig. 6 Reentry heating data for the Mercury MA-5 capsule at three circumferential afterbody thermocouple locations (from Ref. 25).

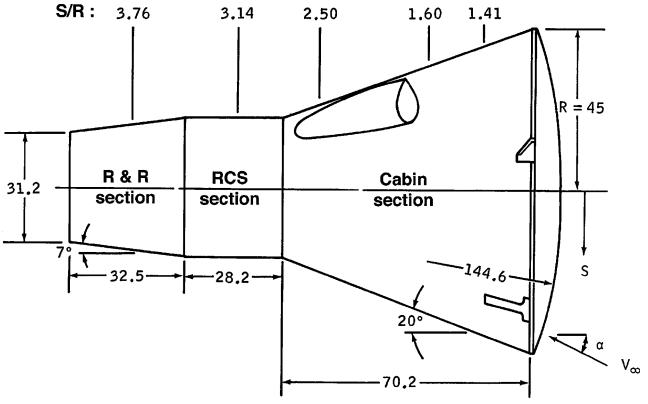

Fig. 7 Schematic diagram of the Gemini capsule reentry configuration (from Ref. 30). All dimensions in inches.

to Big-Joe (Fig. 3), the corrugations on the afterbody are circumferentially oriented. Of the flights for which usable data were obtained, the MA-2 trajectory was designed to produce high afterbody heating rates and was the only nonzero angle of attack entry of the series. Figure 5 shows the measured heat flux at four circumferentially distributed TC locations for MA-2. As seen in Fig. 5, the windward centerline heating rate at these locations is more than a factor of two higher than the leeward centerline, but the leeward heating is somewhat higher than that at the two midplane locations. These data were interpreted as evidence of crossflow separation resulting from the 12.5-deg trim angle of attack.[25] The highest heating rates measured on the afterbody ($\sim$18 W/cm^2) again occurred on the cylindrical section (not shown in Fig. 5). The MA-5 and MA-8 capsules flew nearly identical ballistic trajectories, and the resulting heat transfer data were in excellent agreement. Figure 6 shows the measured heating rates on the MA-5 flight at three TC locations. Both flights exhibited an unusual decrease in heat transfer at these locations about 220 s after entry, as shown in Fig. 6. The reasons for this decrease were not known but were suggested to be flow separation, an unknown interaction with the roll modulation reaction control system (RCS), or shock-layer radiation effects.[25] The highest heating rates for MA-5 and MA-8 ($\sim$9 W/cm^2) occurred on the cylindrical section[25] and were again assumed to be caused by turbulent shear-layer reattachment.

Given the large angle-of-attack oscillations during the heat pulse of the Big-Joe entry, the utility of that flight data for code validation studies is low. The primary concern regarding the utility of the remainder of the Project Mercury flight data is the corrugated afterbody design. The thermocouples for Big-Joe were mounted on the inside of the flat surfaces between the corrugations,[23] whereas those for the Mercury-Atlas flights were mounted at the peaks.[25] In either case the corrugations certainly had an effect on both laminar and turbulent heating levels[26,27] as well as the flow structure in the separated wake. The corrugations may also have influenced transition to turbulence, although comparisons between MA-5 flight data and wind-tunnel transition data[28] suggested that the corrugated surface did not have a large effect on transition.[25] In any case, no known published attempts have been made to simulate the Mercury heating data with modern computational techniques.

B. Gemini Program

The Gemini program used nearly the same capsule outer mold line as Mercury, although it was scaled up somewhat to enable two-person crews. Another primary difference between the Mercury and Gemini spacecraft was that Gemini was designed to fly at a moderate angle of attack via an offset c.g. to generate a small amount of lift ($L/D \sim 0.15$) (Ref. 29). In addition, the forebody heat shield material was changed to a phenolic honeycomb filled with silicone elastomer.[30] Afterbody heat-shield materials were the same as for Mercury, with the exception that the aft cover material was changed from René 41 to beryllium plates because of anticipated high heating rates caused by the angle of attack. The afterbody was coated with a blue-black ceramic paint to increase surface emissivity,[31] which improves the efficiency of reradiation as a heat-rejection mechanism. See Fig. 7 for a schematic of the Gemini reentry capsule.

The main purpose of the first mission, Gemini-Titan 1 (GT-1), was to demonstrate structural integrity and nominal performance during the launch and ascent heating environment. No measurements were made during reentry. The second mission (GT-2) had a primary objective to demonstrate that the vehicle could survive under the most extreme reentry heating conditions and was instrumented with a total of 29 afterbody thermocouples.[30] The third and fourth missions (GT-3 and GT-4) had measurement of flight heating rates as a minor objective only and carried five and eight afterbody thermocouples, respectively.[30] Each capsule also carried eight pressure transducers on the afterbody as well as multiple thermocouples embedded at various depths in the forebody TPS. Instrumentation locations for all three flight vehicles are given in Ref. 30. The thermocouples in the cabin section were welded to the inside of the corrugated

René 41 in a manner analogous to that used for Mercury, whereas those in the reaction control system (RCS) and rendezvous and recovery (R&R) sections were mounted behind the beryllium plates. See Table 1 for a listing of the three Gemini flights with reentry afterbody heating data. Finally, radio-signal attenuation through the ionized wake with and without water injection was measured on the GT-3 flight.[32,33] These data may be useful in validating predictions of electron-number densities in the wake flow.

The only published analysis of these data is given in Ref. 30 and is briefly summarized here. The GT-2 capsule flew a relatively steep ($\gamma = -3$ deg; Ref. 34) simulated abort trajectory and thus experienced heating rates near the design limits of the spacecraft. Heating on the windward side of the afterbody was particularly high because GT-2 also had the largest trim angle of attack ($\alpha = 18$ deg) of the test flights. Heat fluxes up to 12.7 W/cm^2 were measured on the cabin section and 24.9 W/cm^2 (about 25% of the theoretical peak stagnation point heat flux) on the RCS section. Measured afterbody heating rates for GT-2 at 12 thermocouple locations are shown in Fig. 8. Peak forebody heating occurred at about 190 s. The double-humped heating profile on the windward side of the cabin for GT-2 (Fig. 8a) was taken as evidence of transition to turbulence just after peak heating, with the peak turbulent heating rate occurring about 30 s later than peak forebody stagnation-point heating. In addition, the heating on the lee side of the R&R section was about 50% higher than that on the windward side (10.5 vs 7 W/cm^2 [9.2 vs 6 BTU/ft^2 · s]; Figs. 8c and 8d). This anomaly was also seen in high-Reynolds-number wind-tunnel testing and was assumed to be caused by crossflow transition due to the trim angle of attack. Postflight inspection of the GT-2 spacecraft indicated that two small burn-throughs occurred on the RCS section near the umbilical fairings. Because of this discovery the local thickness of the beryllium shingles was increased and the trim angle of attack was lowered on subsequent flights.[31] No clear evidence of transition to turbulence was seen for the GT-3 and GT-4 flights, which had peak measured heating rates on the RCS section of 7 and 11 W/cm^2, respectively.

The primary concern with the utility of the Gemini flight data is the same as for Mercury: the corrugated afterbody surface and the difficulty in assessing its effect on flow structures and heating levels. It should be noted that Raper[30] provides exact locations and flight data only for a subset of the thermocouples and pressure transducers on the three missions. No other sources of flight heating and pressure data from the Gemini program have been located, although an addendum to Ref. 30 indicates that flight data from all thermocouples for GT-2 and GT-3 were available on request from the Manned Spacecraft Center (now Johnson Space Center); these documents may be available through the National Archives and Records Administration (NARA) regional center in Fort Worth, Texas.

C. Project Fire

Project Fire was an Apollo technology demonstrator program that resulted in two ballistic entry test flights, Fire-I[35,36] and Fire-II.[37,38] The Fire-I probe became the first manmade object to enter the Earth's atmosphere at a superorbital velocity when it flew on 14 April 1964. The primary objective of Project Fire was to understand the convective and radiative heating environment of an Earth-entry vehicle at lunar return velocities.[39] The forebody instrumentation included three spherical-section beryllium calorimeters backed by phenolic-asbestos heat shields, as well as two radiometers and a spectrometer package for shock-layer radiation measurements. The forebody was designed such that the first two calorimeters and their backing heat shields could be ejected when their melt temperature was reached, which exposed the pristine calorimeter underneath to the flow and resulted in three distinct flight segments. The ablative silica-phenolic afterbody TPS was instrumented with nine surface-mounted thermocouples, one pressure sensor, and a single radiometer.[38] Table 1 shows the entry conditions for the Project Fire flight tests, and Fig. 9 shows the vehicle geometry and afterbody instrument placement for Fire-II. The nine thermocouples were mounted concentrically in groups of three at three x/L locations (stations) on the afterbody. Finally, each vehicle carried two directional couplers to measure radio-signal attenuation through the ionized wake.[40]

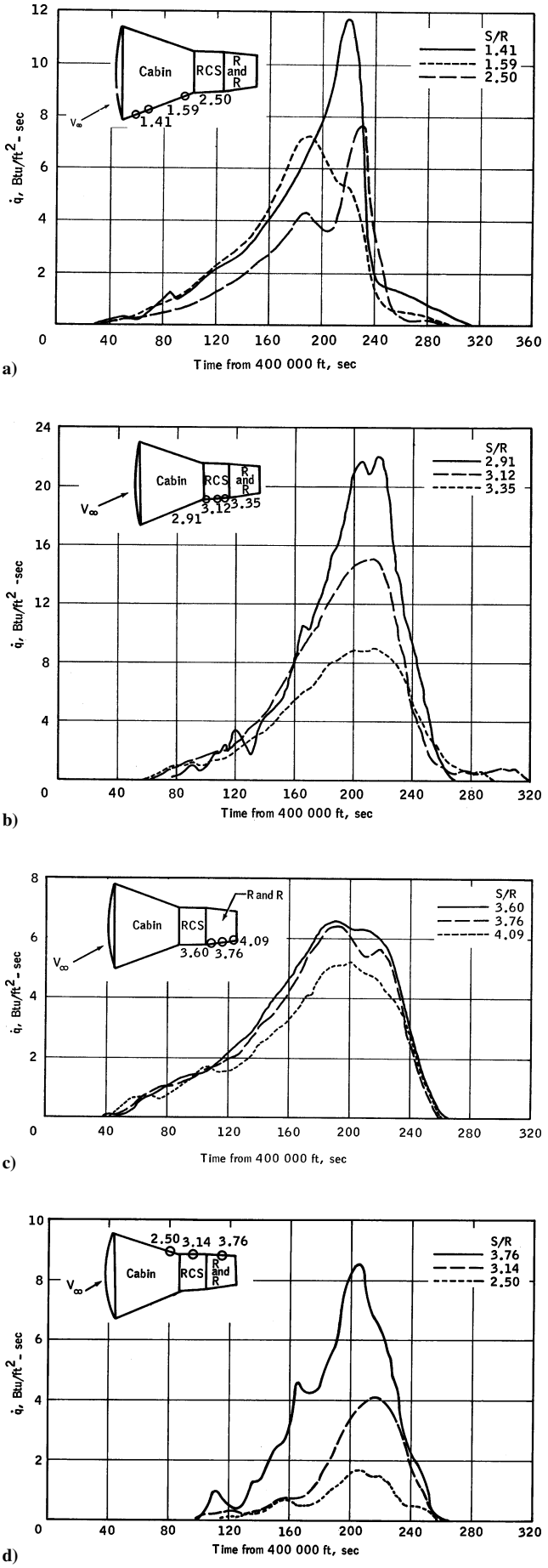

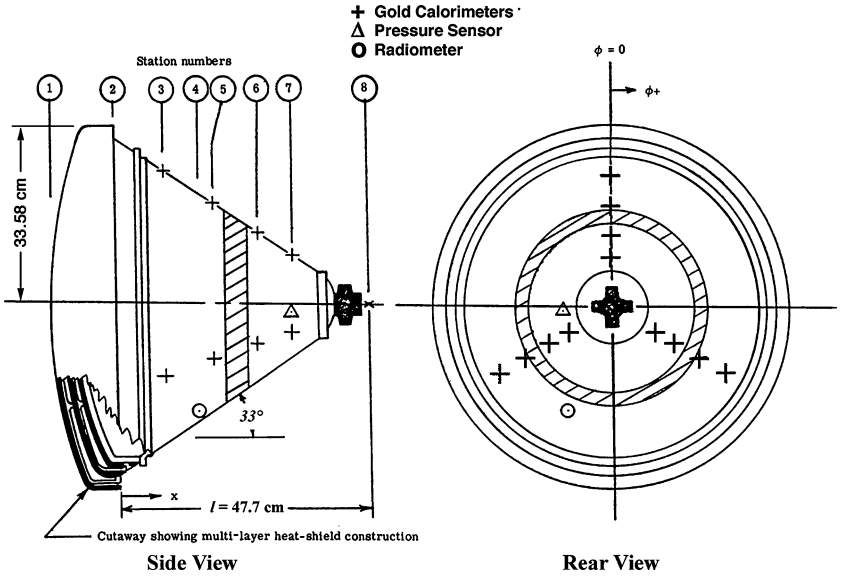

Fig. 9 Schematic diagram of the Fire II reentry vehicle showing instrument placement (from Ref. 38).

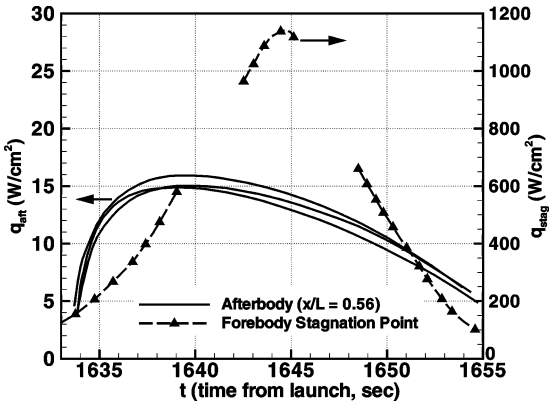

Fig. 10 Time histories of heat transfer measured during the Fire-II flight on the conical afterbody frustum and at the forebody stagnation point (from Ref. 43).

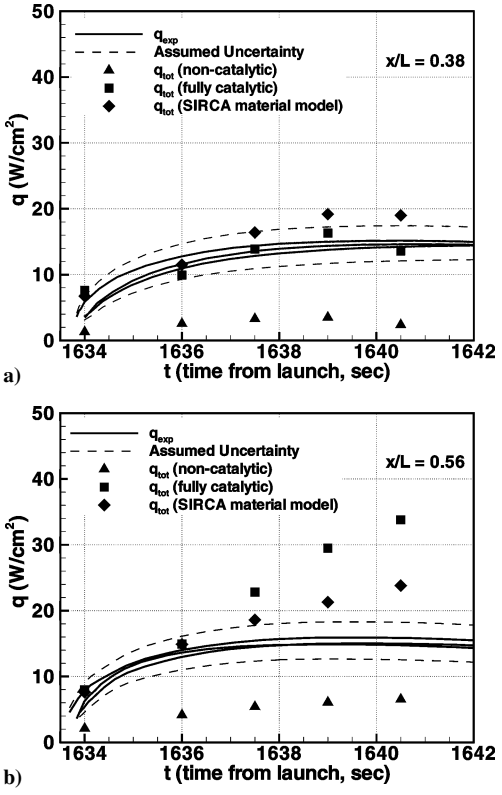

Fig. 11 Time histories of afterbody heat transfer for Fire-II computed using several wall catalysis models (q_{tot}) as compared to flight data (q_{exp}) at two axial locations (from Ref. 43).

Unfortunately, the Fire-I probe experienced large angle-of-attack oscillations during entry, due to a stage-separation anomaly in which the booster entered in front of the capsule.[41] As a result of this anomaly, the shock wave from the booster stage apparently impinged on the Fire-I capsule during a portion of the entry,[41] making the data from this flight very difficult to interpret. In contrast, the Fire-II flight was extremely successful. The vehicle maintained an angle of attack of less than 2 deg through the highest afterbody heating portion of the entry, increasing to about 19 deg by the end of the experiment.[42] All afterbody instrumentation was functional during this flight, providing a valuable database of afterbody heating for a ballistic entry vehicle. Figure 10 shows the time histories of total heat transfer measured during flight by three concentrically mounted thermocouples at one afterbody station on the conical frustum and also at the forebody stagnation point. Peak afterbody heating at this location was about 16 W/cm^2, or 1.5% of the peak stagnation-point heating. The afterbody radiometer was determined to be functional but did not measure any signal during the heating portion of the entry, indicating that radiative heating to the afterbody was negligible at these conditions.[38]

The Fire-II afterbody flight heat transfer data were analyzed in detail by Wright et al.[43] using a nonequilibrium Navier–Stokes CFD code. The CFD results concentrated on the early portion of the trajectory, up to a time just prior to the ejection of the first forebody heat shield. The flowfield during this time was assumed to be axisymmetric, which was consistent with the level of agreement between the heat transfer measurements for three circumferentially mounted calorimeters at each station,[38] as well as the flight-dynamics analysis of Scallion and Lewis.[42] All cases were computed assuming laminar flow, an assumption justified using the free shear-layer transition correlation of Lees.[13] A partially catalytic afterbody surface was assumed, with the catalytic efficiency of the TPS approximated using analogies to similar currently manufactured materials. Figure 11 shows the results of this analysis for two afterbody stations. The computations agreed with the flight data to within the experimental uncertainty over the early portion of the trajectory ($t < 1638$ s). The computations overpredicted the flight data later in the trajectory, especially on the rear of the body (larger x/L), but this result was

attributed to the onset of pyrolysis and ablation of the TPS material, which was not modeled in the simulations.[43] The results demonstrated that modern CFD methods are capable of reproducing the flight data to within experimental accuracy as long as realistic surface boundary conditions are employed. A more recent computation of the later (turbulent) portion of the trajectory using detached eddy simulation (DES) techniques has also been published[44]; however, the computations were preliminary and did not include comparisons to flight data.

D. Apollo Program

The Apollo program sponsored several dedicated flight tests to better understand the heating environment of orbital and superorbital entry probes. Once the design of the Apollo Command Module was determined, four unmanned flight tests were conducted that included forebody and afterbody instrumentation. The first two, Apollo-Saturn 201 (AS-201) and AS-202, reentered at orbital velocities, and the final two, Apollo 4 and Apollo 6, used a kick stage to achieve superorbital entry velocities representative of lunar return. Table 1 shows the relevant entry parameters for these tests. The Apollo Command Module essentially consisted of a spherical section forebody and a 33-deg conical afterbody. The entire surface of the vehicle was covered with Avcoat 5026-39/HC-G, a quartz-fiber-reinforced epoxy resin ablator developed for the Apollo program, which was injected into a phenolic honeycomb matrix that was bonded to the substructure.[45,46] These four flights together constitute the best database of flight afterbody-heating data obtained to date. An onboard inertial measurement unit (IMU) during the last three flights enabled an accurate trajectory reconstruction, and sounding rockets were used to reconstruct atmospheric properties at the time of entry.[47,48] The range of entry velocities and flight-path angles during these flights was sufficient to span multiple flow regimes, from laminar to fully turbulent, and from minimal afterbody material response to strong pyrolysis injection and char formation. This range of conditions will permit a systematic study of the effects of turbulent transition and pyrolysis gas injection on afterbody heating levels.

The afterbody instrument package for AS-201 and AS-202 consisted of 23 surface-mounted calorimeters and 24 pressure transducers.[49] Calorimeter locations are shown in Fig. 12, as are the approximate locations of several afterbody protrusions (antennae and fairings). Both flights were highly successful, with 16 of the calorimeters returning useful data on AS-201 and 19 on AS-202.[49] Pressure data were also obtained during the AS-201 flight, but the dynamic pressure during the AS-202 mission was too low for meaningful pressure readings to be obtained on the afterbody. The afterbody heating rates for AS-201 were much higher than those for AS-202 because of the steeper entry angle (maximum heating rate of 25 vs 9 W/cm^2), and therefore the measured heat

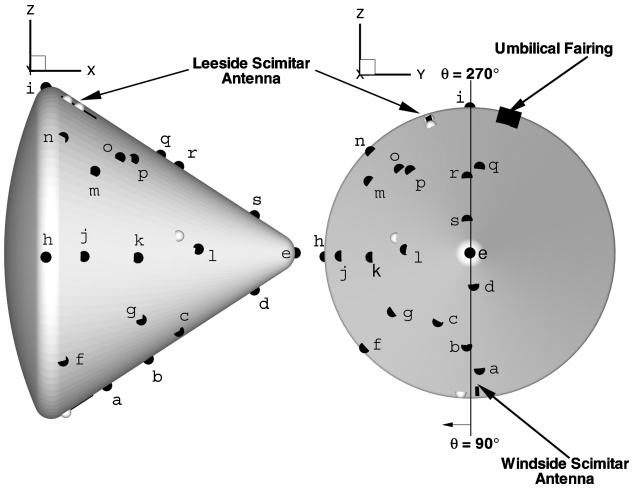

Fig. 12 Calorimeter locations on the AS-201/202 afterbody. Unlabeled symbols indicate inoperative instruments during AS-202 flight (from Ref. 51).

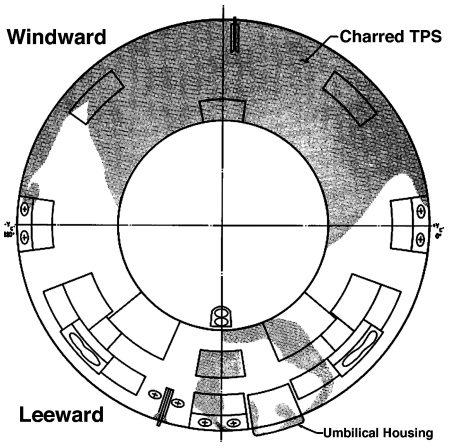

Fig. 13 Schematic diagram of the char pattern on the afterbody of the recovered AS-201 capsule (from Ref. 49). Center white circle represents the portion of the afterbody that is ejected before parachute deployment; the char pattern in this area is unknown.

fluxes for this mission were significantly affected by pyrolysis and charring of the TPS material.[50] Figure 13 shows a schematic of the char pattern on the recovered AS-201 afterbody. Much of the windward side of the afterbody is charred, and some local (mostly minor) charring is visible on the leeward side near the umbilical housing. The rear portion of the capsule was ejected prior to parachute deployment; therefore no charring in this area is indicated in Fig. 13. The char pattern on AS-201 is slightly asymmetric because of an unanticipated roll angle during the entry.[50] In contrast, the afterbody of the recovered AS-202 capsule showed little evidence of charring.[50] However, many of the calorimeters mounted near RCS exhaust ports experienced large transient spikes in heat transfer that were tied to thrusting events[49]; these data may be useful in understanding the importance of RCS interactions on local aeroheating.

The afterbody heating data for AS-201 have not been investigated in detail using modern CFD methods. However, a recent paper analyzed the flight data for AS-202.[51] A total of 15 three-dimensional nonequilibrium Navier–Stokes CFD solutions were run, spanning the time from the onset of continuum flow until the separation region became unsteady. The surface was assumed to be fully catalytic, which was a reasonable assumption for the hydrocarbon-resin-based Avcoat TPS material. The results were computed assuming laminar flow, again validated using the correlation of Lees.[13] The computations generally agreed with the flight data to within the experimental uncertainty ($\pm 20\%$) for 15 of the 19 functional calorimeters.[51] The results at three afterbody calorimeter locations are shown in Fig. 14. The first (calorimeter a) was in an attached flow region, the second (m) was in separated flow, and the third (j) was at a location where the flow transitioned from separated to attached during the entry. The heat pulse has two distinct lobes due to an atmospheric skip maneuver performed by the spacecraft during entry. Interestingly, both the flight data and the CFD results at calorimeter j clearly show the reattachment at $t = 4600$ s and separation at $t = 4800$ s, which indicates that the CFD solutions are accurately predicting not only the magnitude of the heating but also the extent of separation. The overprediction in heating at calorimeter a near $t = 4700$ s was thought to be due to noncontinuum effects near the peak (high-altitude point) of the skip-out maneuver.[51] The predicted heating during the second peak at calorimeter m (and several other locations) was significantly below measured values; this was postulated to be due to transition to turbulence at about $t = 4900$ s (Ref. 51). Relatively poor agreement was obtained for two calorimeters near the rear apex of the vehicle; the reason is not known at this time but it may be due to unmodeled details of the apex geometry. This work again demonstrated the ability of modern computational methods to accurately predict afterbody-heating levels, this time for a lifting body.

The Apollo 4 and 6 test flights were intended to qualify the entry system for lunar return by entering at $\alpha = 25$ deg and a relative

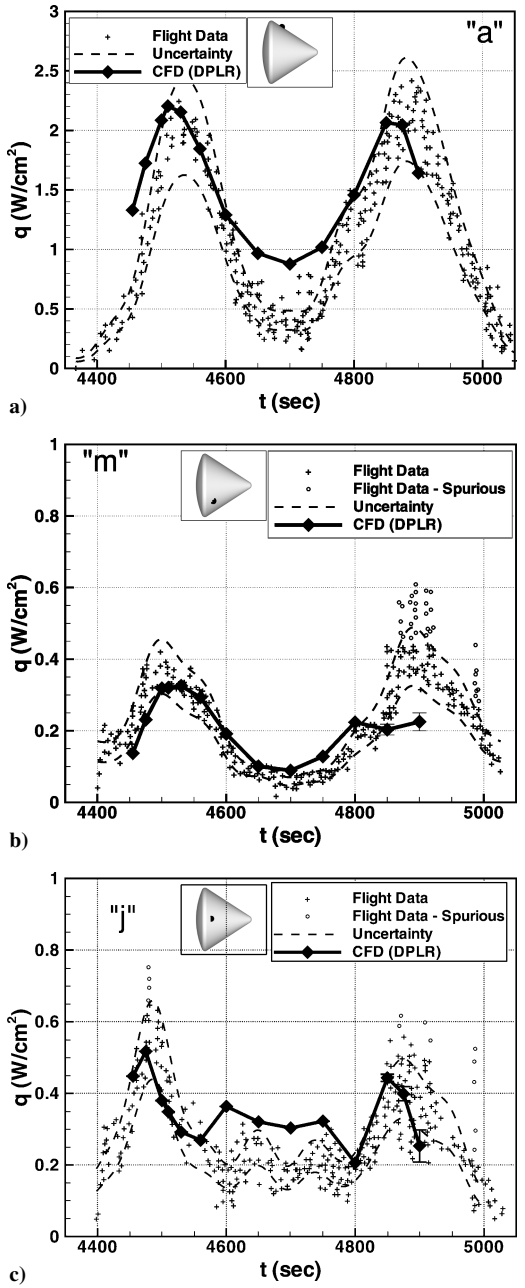

Fig. 14 Comparison of flight data and computed heat transfer at three calorimeter locations on the afterbody for AS-202. Letters indicate calorimeter ID in Fig. 12 (from Ref. 51).

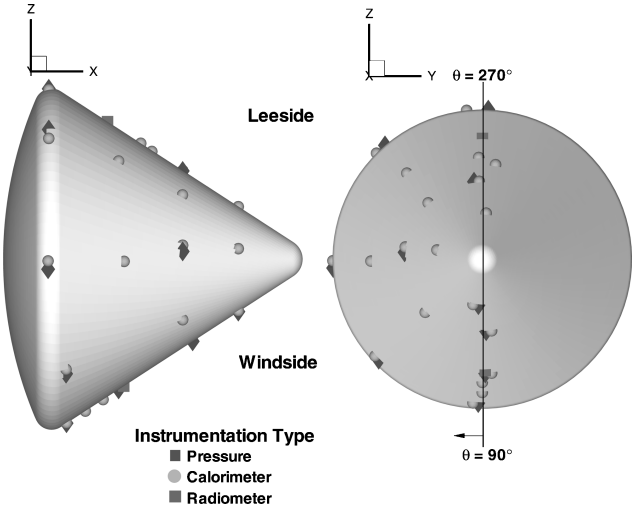

Fig. 15 Instrumentation locations on Apollo 4 and Apollo 6 conical afterbody.

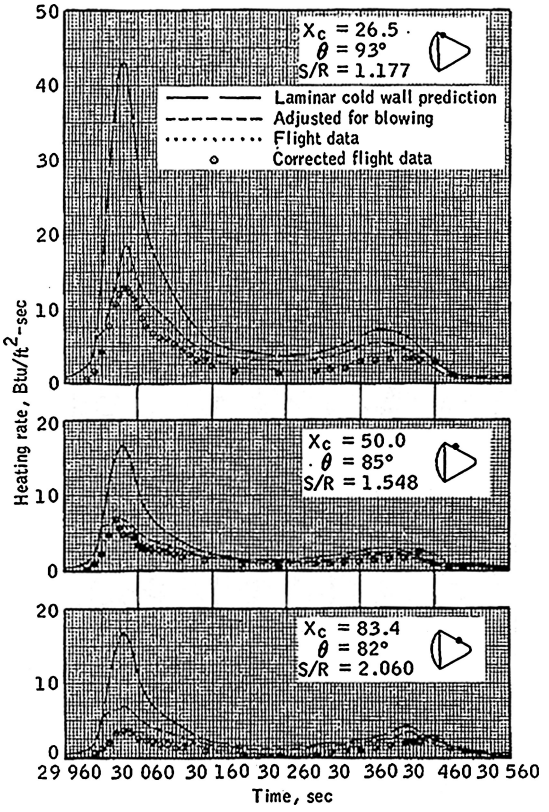

Fig. 16 Flight data and preflight engineering predictions from the Apollo 4 entry at three calorimeter locations on the attached flow portion of the afterbody (from Ref. 52).

velocity of about 11 km/s. The actual entry velocity for Apollo 6 was only about 9.6 km/s because of a reignition failure in the upper stage.[52] The afterbody instrument package was modified for these flights and consisted of 21 calorimeters, 10 pressure transducers, and 2 radiometers. The locations of the instrumentation for Apollo 4 and 6 are shown in Fig. 15. All 21 calorimeters provided useful data on each flight. Four of the calorimeters were placed near simulated protuberances and gaps in the flight vehicle; these data, along with similar data obtained via sounding rocket tests,[53] may be useful to validate the ability of modern CFD to predict local heating around geometrical singularities. The remaining calorimeters provided flight data of afterbody heat transfer on an ablating TPS material. The afterbody radiometers for both flights failed to detect a measurable signal, although they were determined to be functional. This result confirmed preflight predictions of negligible radiative heating[54] and implies that there was zero afterbody radiative heating on the lower velocity AS-201 and AS-202 flights as well. There was little charring on the separated flow portion of the afterbody, and total heating levels in the separated flow region were between 1–2% of the theoretical forebody stagnation-point value. The pressure and total heat transfer measured on the charred (attached flow) regions of the afterbody were corrected for wall blowing, but the resulting heat transfer rate was significantly lower than the preflight computations (Fig. 16) for both flights. The level of underprediction was determined to be proportional to the forebody heating rate. Although a definitive reason for this effect has not been identified, it has been postulated that the cause was upstream blowing of ablation products into the boundary layer.[3,52,55] The afterbody-heating data from these flights have yet to be looked at in detail with modern computational methods.

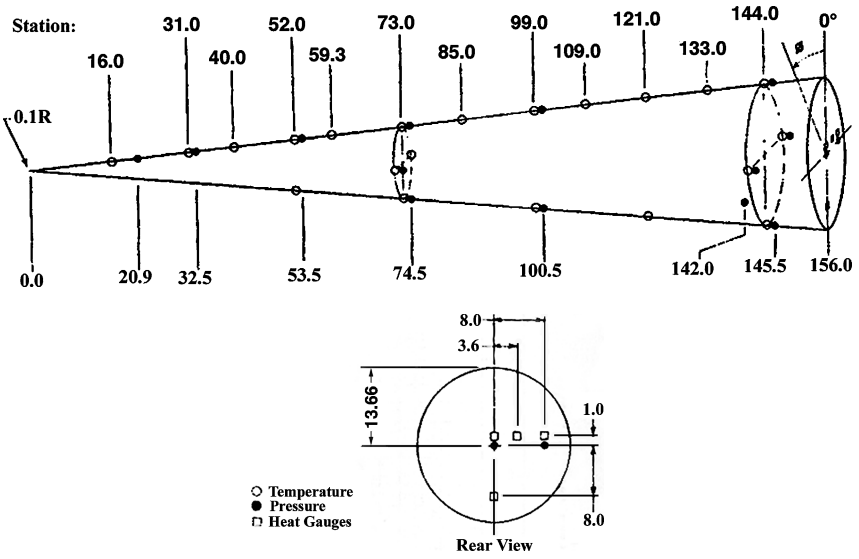

Fig. 17 Schematic diagram of the Reentry F test vehicle showing instrument locations on the cone and base (from Ref. 60). All dimensions in inches.

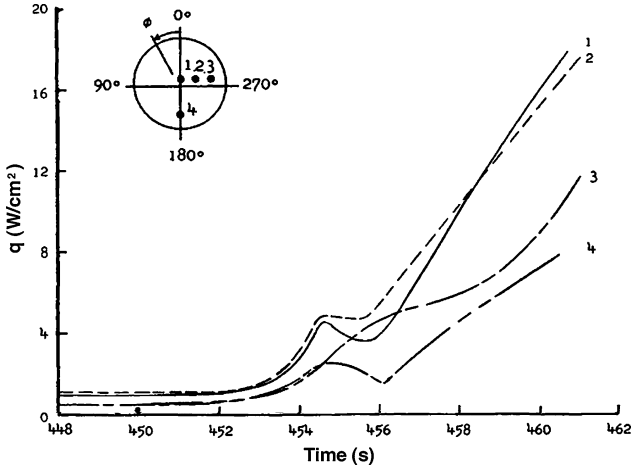

Fig. 18 Measured heat transfer rates at all four afterbody calorimeter locations for Reentry F (from Ref. 60).

E. Reentry F

The Reentry F flight test was launched on 27 April 1968, from Wallops Island and entered at a relative velocity of 6 km/s on a ballistic trajectory.[56] The entry vehicle was a 3.92-m-long, 5-deg-half-angle beryllium cone with a graphite nose tip and was designed to provide free-flight transition and turbulent heat transfer data.[57] Similar data were also obtained via sounding-rocket-launched ablative slender cones.[58,59] The base cover consisted of a glass-phenolic bulkhead with stiffening members surrounded by a rubber-coated stainless-steel rim cover and included quartz windows for telemetry transmissions.[60] The cone was instrumented with thermocouples and pressure sensors at 21 measurement stations, and the base had a total of 4 heat flux and 4 pressure sensors.[56] Instrument locations are shown in Fig. 17. Two pressure sensors were placed at each location shown in Fig. 17; one for low-pressure (0–690 Pa) and one for high-pressure (0–6900 Pa) measurements.[57] The final reconstructed entry trajectory for Reentry F is presented in Ref. 61. Atmospheric properties were determined with balloon and sounding-rocket flights before the Reentry F test.[56] Postflight analysis of these data was somewhat complicated by thermal distortions of the metal structure, which resulted in a small effective angle of attack of as much as 1.0 deg late in the flight.[62,63]

Afterbody flight data and comparisons to analytical methods were presented in Ref. 60. Figure 18 shows the measured heating rates at all four calorimeter locations as a function of time. Late in the entry (when the flow is turbulent) the heat flux on the base appears to be about 30% higher near the centerline (calorimeters 1 and 2) than at the two most off-axis locations (calorimeters 3 and 4). In contrast, all four calorimeters predict nearly the same heating rate early in the entry (laminar flow region). This is in contrast to the measured base pressure, which was nearly constant in the turbulent flow regime but was higher near the center of the base for laminar flow.[60] All four calorimeters show an unusual fall in heat flux at about $t = 454$ s. The reasons for this fall are not currently known, but it was noted that this point corresponds closely to the time when angle of attack started to increase due to thermal distortions.[60] Figure 18 also shows that the heat flux at all calorimeter locations rises rapidly after $t = 455$ s, which was taken to be indicative of transition to turbulence on the base. Peak heat fluxes of about 18 W/cm^2 were experienced at about $t = 462$ s. These data should be an excellent resource for flight validation of predictions of heat flux to the flat base of nominally axisymmetric ballistic entry vehicles. However, to date no comprehensive analysis of the afterbody data has been attempted with modern CFD tools.

F. Mars Viking I and II

The Viking program included two landers that entered the Martian atmosphere in July and September 1976. Both probes were 70-deg sphere-cones with an ablative forebody heat shield made of a lightweight silicone-based ablator called SLA-561, which was injected into a phenolic fiberglass honeycomb structure. The Viking probes flew a lifting entry at a nominal angle of attack of 11 deg and entered at a relative velocity of about 4.5 km/s (Ref. 64). Atmospheric properties along the reconstructed flight trajectories are given by Seiff and Kirk.[65] Unlike subsequent Mars missions, both Viking landers descended from orbit rather than entering hyperbolically, in part because of concerns about the severity of the entry heating environment. Each probe included a base pressure sensor and two surface-mounted aftbody temperature sensors: one on the fiberglass inner cone and one on the aluminum skin of the outer cone.[66] A schematic of the Viking entry probe showing the afterbody temperature sensor locations is given in Fig. 19. The base pressure sensor was actually inside the aeroshell, which was vented. Three of the four temperature sensors worked fine, but the sensor on the aluminum outer cone of the Viking I entry vehicle failed near the peak heating point.[66]

Preflight analysis predicted afterbody heating to be 3% of the forebody stagnation point heating rate,[66] but flight data indicated that the peak heating was actually more than 5% of the stagnation value, as shown in Fig. 20. The high heating levels, as well as the slope change observed in heating rate vs Reynolds number

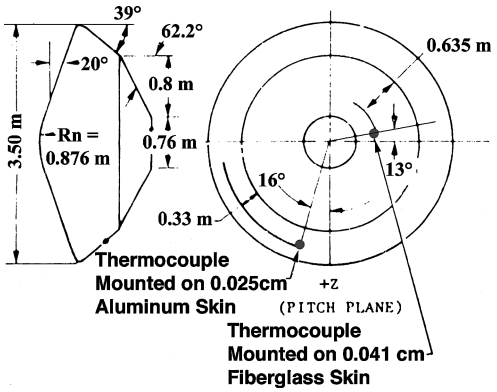

Fig. 19 Schematic of Viking entry configuration showing afterbody thermocouple locations (from Ref. 67).

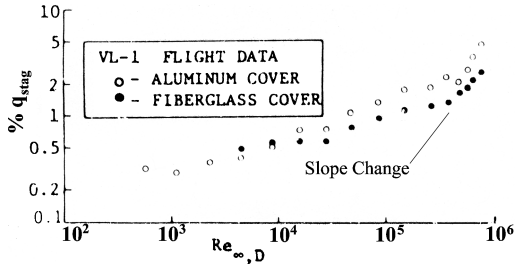

Fig. 20 Flight data from the afterbody temperature sensors on Viking 1 (from Ref. 66).

at $Re_D \sim 5 \times 10^5$, were believed to be evidence of turbulent transition on the base.[67] Transition, as determined by the slope change in Fig. 20, occurred at approximately the same time as the peak forebody stagnation-point heating rate on the trajectory.

Although the Viking heat transfer data are the first afterbody flight data for any non-Earth entry, the first published attempt to reproduce these data with modern CFD techniques was not completed until recently. Edquist et al.[68] reanalyzed the thermocouple data, including the effects of internal heating from the on-board Radioisotope Thermoelectric Generators (RTGs), and explored the impact of material response and entry trajectory uncertainties on the resulting measured heating rates. In addition, detailed CFD simulations were performed with two different codes at 11 points along the entry trajectory for the Viking I lander.[68] The results of this analysis indicated that the wake flowfield was predicted to be unsteady even at low Reynolds number, apparently due to the sharp shoulder radius of the Viking aeroshell.[68] Owing to the unsteady nature of the predicted flowfield, the CFD results were first averaged and then compared to the flight data at the two thermocouple locations. As shown in Fig. 21, the computational results generally underpredict the measured heating rates (by as much as a factor of five), particularly on the aluminum base cover near the peak heating point. At this time the reasons for this discrepancy are not known.

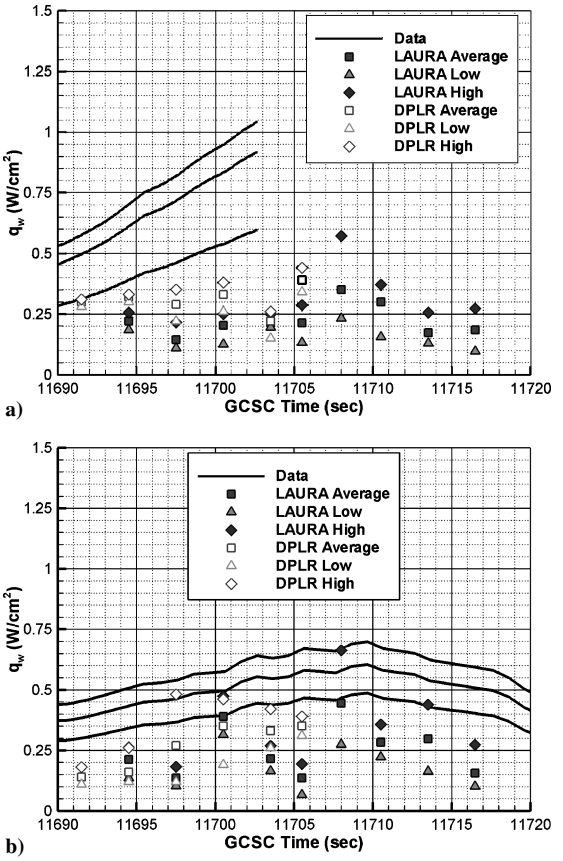

Fig. 21 Comparison of flight data and computed heat transfer on the afterbody for Viking I: a) thermocouple in the aluminum cone and b) thermocouple in the fiberglass cone (from Ref. 68).

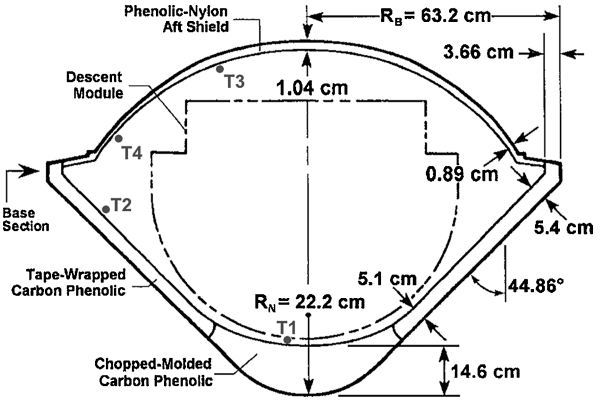

Fig. 22 Schematic of Galileo probe with thermometer locations marked (adapted from Ref. 72).

G. Galileo

The Galileo mission was launched 18 October 1989. The onboard 45-deg sphere-cone probe successfully entered the Jovian atmosphere on 7 December 1995, on a ballistic trajectory at a relative velocity of 47.4 km/s (Ref. 69). This probe survived the most severe heating environment ever experienced by a planetary-entry capsule, with a peak ablating heat flux on the order of 17 kW/cm^2. The forebody heat shield was constructed of fully dense carbon phenolic, and the aftshell was made of a lower density phenolic-nylon material.[70] Instrumentation consisted of 10 analog resistance ablation (ARAD) sensors on the forebody and 4 resistance thermometers bonded to the structure beneath the TPS,[70] as shown in Fig. 22. Each thermometer was sampled every 8 s during the entry, and only six values for each were stored. Although the temperature measurements were intended to stop at the same time as the recession measurements ($t = 110$ s), the stop command was never issued because of a software glitch.[71] Therefore, the early entry data were all overwritten (including the initial cold-soak temperatures) and data were stored from about $t = 120$ to 160 s (Ref. 72). Both afterbody thermometers (T3 and T4 in Fig. 22) appeared to function normally.

Considerable effort was spent on predicting the base heating environment of the Galileo probe during the design phase.[73,74] However, the only postflight analysis of these data to date was performed by Milos et al.,[72] who simulated the thermometer response using a transient material response code coupled to a finite element thermal analysis package. CFD analysis of the external flowfield was not performed. Instead, a triangular heat pulse was assumed with a total heat load based on engineering predictions. The results in Ref. 72 indicate that the postflight analysis was not in good agreement with

the afterbody flight data. Although it was possible to bound the flight data by varying the applied heat load and the initial cold-soak structural temperature, the rate of temperature increase predicted by Milos et al.[72] at both T3 and T4 was much higher than that observed in flight. It remains to be seen whether a high-fidelity aerothermal analysis could improve the agreement with the flight data, although it should be noted that the Galileo entry flowfield is an extremely complex mix of optically thick shock-layer radiation, highly ionized plasma, strong ablation, and turbulent flow. Any one of these effects would be difficult to simulate; all of them together present a significant challenge to the state-of-the-art CFD methodology. The results of the ARAD forebody heat-shield recession experiment, as reported in Ref. 75, indicated that recession at the nose was much less than predicted, whereas recession on the flank was much greater, nearly leading to burn-through. The reasons for this discrepancy are still not known, although recent theories proposed by Tauber[76] and Matsuyama et al.[77] are promising. It is likely that resolution of the afterbody heating will not be possible until the forebody environment is better understood.

H. Mars Pathfinder

Mars Pathfinder was launched 4 December 1996, and successfully entered the Martian atmosphere on July 4, 1997, on a ballistic trajectory at a relative velocity of 7.5 km/s (Ref. 78). The forebody TPS for this mission was SLA-561V, nearly identical to that employed on Viking. The afterbody frustum was coated with SLA-561S (a spray-on version of SLA-561V).[79] The backshell interface plate (BIP) and the rear portion of the frustum were covered with SIRCA (silicon-impregnated reusable ceramic ablator) tiles.[80] There was no surface-mounted instrumentation, but the aeroshell did contain nine TCs at various depths in the TPS material and three platinum resistance thermometers (PRTs) as shown in Fig. 23. PRT2 and PRT3 were mounted to aluminum blocks inside the structure and were used only to provide a reference calibration point for the TC data. Of the instrumentation on the afterbody, usable data were obtained from TC9, PRT1, and PRT3. Time histories of the temperature data at these locations are given in Ref. 80.

The only postflight analysis of these data to date was performed by Milos et al.[80] In this analysis afterbody heating estimates were scaled from forebody CFD solutions rather than computed directly. Using this assumption, Milos et al.[80] were able to reproduce the peak temperature at TC9 but not the time history of the temperature response. However, by generating a best-fit heating profile with a maximum heat flux of 1.3 W/cm^2 that was longer in duration than the scaled forebody profile, they were able to demonstrate excellent agreement with the flight data. The assumed shape of the best-fit profile was in general agreement with preflight predictions,[81,82] but the heating rates required to match the flight data were considerably lower. To our knowledge no attempt has been made to reconcile this discrepancy. It is also worth noting that Sojourner rover photographs of the aftshell on the surface of Mars showed that the BIP apparently

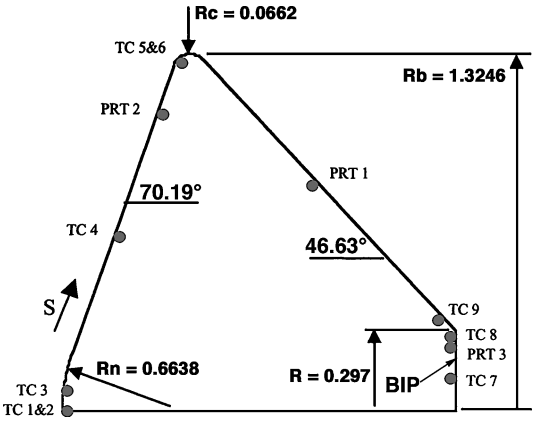

Fig. 23 Mars Pathfinder schematic showing instrument locations (from Ref. 80). Instruments are not coplanar.

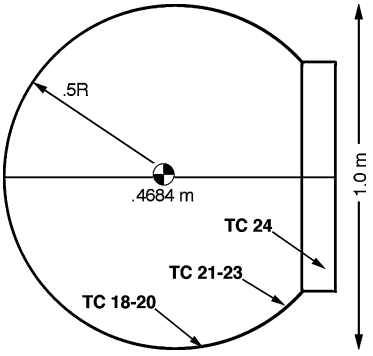

Fig. 24 Schematic of the MIRKA capsule with approximate location of afterbody thermocouples.

remained white.[80] This indicates that surface temperature on the BIP never exceeded about 800 K, the point at which char starts to form on SIRCA.[83]

I. MIRKA

The MIRKA capsule was a German-led, low-cost flight experiment flown as a piggyback payload on a Russian FOTON. MIRKA successfully reentered the Earth's atmosphere on a ballistic trajectory at a velocity of 7.6 km/s on 23 October 1997.[84] The capsule, shown schematically in Fig. 24, was essentially a 1-m-diam sphere with a flat base. The capsule was instrumented with 2 pyrometers, 3 rarified flow experiment (RAFLEX) pressure probes, and 25 TCs integrated into the TPS material at various depths.[84] A total of 7 TCs were on the afterbody. The forebody TPS was a material called surface-protected ablator (SPA), which was an Apollo-like ablative material covered by a shell of silicon-carbide (SiC). The pyrolysis gases generated on the forebody could not penetrate the SiC shell but were instead vented at the 90-deg point on the sphere. Several simulations of the MIRKA flight data have been published,[85–87] although these researchers have dealt only with the forebody flow. It was noted in Ref. 85 that the heat-flux readings at TCs 15–17 were strongly influenced by hot pyrolysis gases injected upstream of that location, and it seems likely that those further downstream would also be affected. In addition, the spacecraft underwent some tumbling during the entry, and there was no onboard IMU to accurately determine angle of attack as a function of time, which makes detailed analysis of the afterbody flowfield very difficult (M. Fertig, personal communication, Oct. 2004).

J. Atmospheric Reentry Demonstrator

The ESA launched the Atmospheric Reentry Demonstrator (ARD) on 12 October 1998.[88] The probe reentered the Earth's atmosphere at a relative velocity of 7.5 km/s. ARD was a subscale Apollo-like capsule (shown schematically in Fig. 25) with a diameter of 2.8 m and a rear cone angle of 33 deg. The reconstructed flight trajectory and vehicle aerodynamics are given in Ref. 89. The capsule afterbody was instrumented with seven surface pressure sensors, two thermal plugs with two thermocouples each on the back cover, and four surface-mounted copper calorimeters on the cylindrical section.[90] The locations of the four calorimeters in the cylindrical section are given in Table 2. In Table 2 the circumferential angle θ is measured from the windward centerline and the calorimeter ID is as reported in Ref. 90. Figure 26 shows a photograph of the conical afterbody of the ARD capsule after recovery with two of the calorimeter locations indicated. The forebody TPS consisted of tiles of Aléastrasil (an ablative material containing silica fibers impregnated with phenolic resin), and the afterbody TPS was Norcoat-Liége (cork powder and phenolic resin).[91] There were also five TPS coupons of other materials on the forebody. In addition, the afterbody conical section was coated with thermosensitive paint. The ARD flight test was the first of a tiled ablating thermal protection system, a technology later employed on the ESA Huygens probe, which successfully entered the atmosphere of Titan on 14 January 2005.

No useful data were obtained from the afterbody pressure sensors during the hypersonic portion of the entry because the transducers

Table 2 Calorimeter locations on the afterbody cone of ARD

ID	s/D	θ, deg	r, m
F8	0.805	356.5	1.01807
F9	0.88	356.5	0.8915
F28	0.686	315	1.19802
F29	0.686	45	1.19802

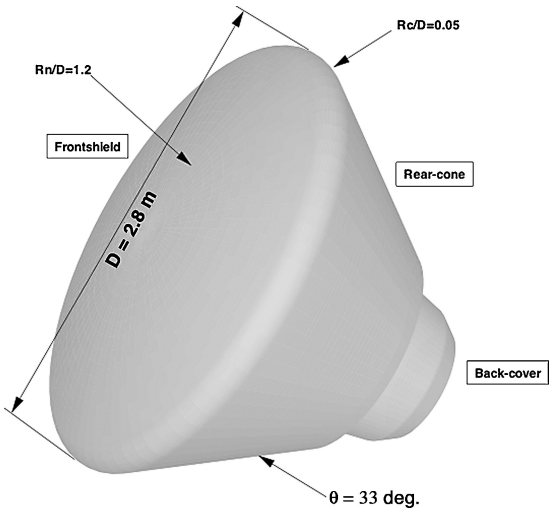

Fig. 25 Schematic of the ARD capsule (from Ref. 90).

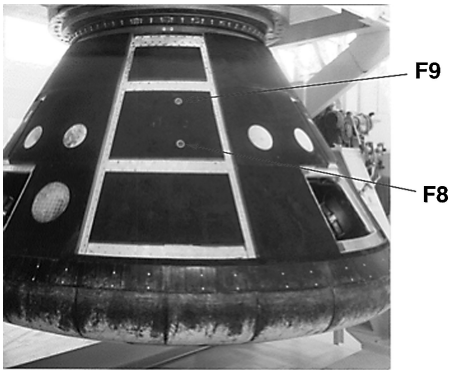

Fig. 26 Postflight photograph of the ARD capsule, showing the locations of two calorimeters (F8 and F9) on the conical afterbody.

were not sensitive enough to measure the low flight pressures with accuracy.[92] Although the forebody thermocouples failed above about 800°C, those on the afterbody were functional throughout the entry. Unfortunately, the deduced heat transfer is not considered to be reliable.[90] Better results were obtained from the calorimeters on the conical section, which provided heat transfer data throughout the entry.[90] Heating rates at each of the four calorimeter locations extracted from the flight data are shown in Fig. 27. The peak heating at all four locations reached about 3.5–4 W/cm^2. Computational analysis of the ARD conical afterbody data has been presented in Ref. 90. Although good agreement was obtained between the computations and flight data early in the trajectory, the fully turbulent CFD calculations (using a Baldwin–Lomax model) overpredicted the peak flight heating by as much as a factor of two, whereas the laminar computations underpredicted the flight data. One possible reason for this discrepancy is inadequacy of the Baldwin–Lomax turbulence model in a (possibly transitional) separated flow. It was also suggested that the finite-rate gas chemistry model might be inaccurate in this region.[91]

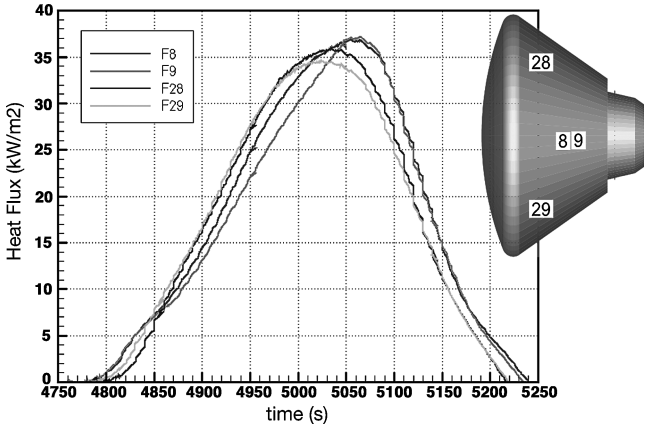

Fig. 27 Flight heating data from the four calorimeters on the conical afterbody of the ARD capsule (adapted from Ref. 90).

IV. Recommendations

Little work has been done to date on understanding turbulent or ablating reentry wake flows. Data from Reentry F, a flat-based ballistic entry vehicle, may help to determine our ability to predict laminar and turbulent heating on a flat base. The Apollo 4 and 6 flight data include the effects of both ablation and turbulence and will allow us to validate current methodologies in this environment. All of these data sources should allow the validity of available afterbody flow transition models to be determined. The lessons learned from this analysis should significantly reduce current uncertainty levels in flight afterbody-heating predictions, leading to improved (lower mass) afterbody TPS on future missions. This work should be completed before recommending new dedicated flight testing so that we are better able to assess the gaps in our ability to predict Earth-entry afterbody heating.

The state of affairs for other planetary destinations is not as good. Although code validation with Earth-entry data certainly increases confidence in our ability to predict afterbody heating at other planets, differences in atmospheric composition and the associated chemical kinetics can only be fully resolved with in situ flight data. Unfortunately, two thermocouples on Viking and a single near-surface thermocouple on Pathfinder are the only truly usable pieces of afterbody flight aeroheating data for any non-Earth entry. To date, neither of these data sources has been fully examined using modern computational tools; this analysis should be a high priority activity for the selection and sizing of the afterbody TPS for future Mars missions.

Finally, we note that although the results presented herein clearly demonstrate the utility of flight data for code validation, the recent trend has been a reduction or even elimination of heat-shield instrumentation as a cost-saving or (perceived) risk-reduction measure. For example, there was no heat-shield instrumentation on the Mars Exploration Rover entry vehicles, the Genesis and Stardust sample return capsules, or the European Mars Beagle or Huygens Titan probes. Future planetary entry vehicles must include heat-shield instrumentation if we wish to improve our understanding of these environments and thereby reduce TPS mass and/or risk on future missions. The aftshell is often the safest place to incorporate instrumentation because of the low heating rates; the results summarized in this paper give increased confidence in our ability to use such data effectively for code validation and improvement.

V. Conclusions

The Mercury and Gemini programs included a total of eight test flights from which afterbody aeroheating and pressure data were obtained. Although of significant historical interest, the utility of the data from these flights is somewhat compromised by the corrugated afterbody surface employed, which would likely be difficult to accurately model because of complex fluid dynamics and multidimensional conduction effects. In contrast, the data obtained during Project Fire and the Apollo program provide an invaluable resource

for the validation of modern computational tools for afterbody aeroheating. The six flight tests provide data spanning the entire range of Earth-entry conditions, from axisymmetric to three dimensional, noncontinuum to continuum, laminar to turbulent, and nonablating to fully ablating. The European ARD flight, together with the American Reentry F, are additional valuable resources for Earth-entry base heating. Recent papers have looked at Fire-II, Apollo AS-202, and ARD flight heating data and have shown that modern computational methods appear to be fully capable of predicting afterbody heating to within the uncertainty of the flight data, at least for laminar flows without ablation. Limited data also exist for afterbody heating from the Pathfinder mission at Mars and the Galileo entry to Jupiter. None of these non-Earth-entry data have yet been examined in detail using full-body CFD analysis.

Acknowledgments

This work was funded by the In-Space Propulsion program under task agreement M-ISP-03-18 to NASA Ames. The authors thank Michelle Munk (NASA Langley) for her unwavering support of this work, Steve Schneider (Purdue University) for useful discussions leading to information on flight data for Project Mercury, and Marcus Fertig (University of Stuttgart) for discussions about the MIRKA flight.

References

[1]Jones, J. J., and Moore, J. A., "Shock Tunnel Heat Transfer Investigation on the Afterbody of an Apollo-Type Configuration at Angles of Attack to 45°," NASA TM X-1042, Dec. 1964.

[2]Zappa, O., and Reinecke, W., "An Experimental Investigation of Base Heating on Typical Mars Entry Body Shapes," NASA CR-1920, Nov. 1971.

[3]Yee, L., "Free-Flight Measurements of Heat Transferred to the Apollo Afterbody with and Without Heat Shield Ablation," NASA TM X-1096, April 1965.

[4]Anderson, J. D., *Hypersonic and High Temperature Gas Dynamics*, McGraw–Hill, New York, 1989, pp. 20–23.

[5]Boyd, I., Chen, G., and Candler, G., "Predicting Failure of the Continuum Fluid Equations in Transitional Hypersonic Flows," *Physics of Fluids*, Vol. 7, No. 1, 1995, pp. 210–219.

[6]Dogra, V., Moss, J., Wilmoth, R., Taylor, J., and Hassan, H., "Effects of Chemistry on Blunt Body Wake Structure," *AIAA Journal*, Vol. 33, No. 3, 1995, pp. 463–469.

[7]Moss, J., and Price, J., "Review of Blunt Body Wake Flows at Hypersonic Low Density Conditions," AIAA Paper 96-1803, June 1996.

[8]Gnoffo, P. A., "Planetary Entry Gas Dynamics," *Annual Review of Fluid Mechanics*, Vol. 31, 1999, pp. 459–494.

[9]Kim, M., Loellbach, J., and Lee, K., "Effects of Gas Models on Hypersonic Base Flow Calculations," *Journal of Spacecraft and Rockets*, Vol. 31, No. 2, 1994, pp. 223–230.

[10]Grasso, F., and Pirozzoli, S., "Nonequilibrium Effects in Near Wake Ionizing Flows," *AIAA Journal*, Vol. 35, No. 7, 1997, pp. 1151–1163.

[11]Olynick, D., Chen, Y.-K., and Tauber, M., "Aerothermodynamics of the Stardust Sample Return Capsule," *Journal of Spacecraft and Rockets*, Vol. 36, No. 3, 1999, pp. 442–462.

[12]Gnoffo, P., Gupta, R., and Shinn, J., "Conservation Equations and Physical Models for Hypersonic Air Flows in Thermal and Chemical Nonequilibrium," NASA TP-2867, Feb. 1989.

[13]Lees, L., "Hypersonic Wakes and Trails," *AIAA Journal*, Vol. 2, No. 3, 1964, pp. 417–428.

[14]Zeiberg, S. L., "Transition Correlations for Hypersonic Wakes," *AIAA Journal*, Vol. 2, No. 3, 1964, pp. 564, 565.

[15]Tauber, M. E., "A Review of High-Speed Convective Heat Transfer Computation Methods," NASA TP-2914, July 1989.

[16]Reda, D. C., "Review and Synthesis of Roughness-Dominated Transition Correlations for Reentry Applications," *Journal of Spacecraft and Rockets*, Vol. 39, No. 2, 2002, pp. 161–167.

[17]Demetriades, A., Laderman, A., Von Seggern, L., Hopkins, A., and Donaldson, J., "Effect of Mass Addition on the Boundary Layer of a Hemisphere at Mach 6," *Journal of Spacecraft and Rockets*, Vol. 13, No. 8, 1976, pp. 508, 509.

[18]Schneider, S. P., "Laminar-Turbulent Transition on Reentry Capsules and Planetary Probes," AIAA Paper 2005-4763, June 2005.

[19]Gnoffo, P., Price, J., and Braun, R., "Computation of Near Wake Aerobrake Flowfields," *Journal of Spacecraft and Rockets*, Vol. 29, No. 2, 1992, pp. 182–189.

[20]Baber, H., Carter, H., and English, R., "Flight Test of a Little Joe Boosted Full-Scale Spacecraft Model and Escape System for Project Mercury," NASA TM X-629, May 1962.

[21]Swenson, L., Grimwood, J., and Alexander, C., "This New Ocean: A History of Project Mercury," NASA SP-4201, 1966.

[22]Space Task Group, "Project Mercury Preliminary Flight Test Results of the Big Joe Mercury R&D Capsule," NASA TM X-73017, Nov. 1959.

[23]Stephens, E., "Afterbody Heating Data Obtained from an Atlas Boosted Mercury Configuration in a Free Body Reentry," NASA TM X-493, Aug. 1961.

[24]O'Neal, R., and Rabb, L. "Heat Shield Performance During Atmospheric Entry of Project Mercury Research and Development Vehicle," NASA TM X-490, May 1961.

[25]Murphy, J. D., "Flight Test Aerodynamic Heating Data for the Afterbody of the Project Mercury Spacecraft with Comparisons to Available Prediction Methods," NASA CR-649, June 1967.

[26]Brandon, H. J., Masek, R. V., and Dunavant, J. C., "Aerodynamic Heating to Corrugation Stiffened Structures in Thick Turbulent Boundary Layers," *AIAA Journal*, Vol. 13, No. 11, 1975, pp. 1460–1466.

[27]Bertram, M. H., Weinstein, L. M., Cary, A. M., and Arrington, J. P., "Heat Transfer to a Wavy Wall in Hypersonic Flow," *AIAA Journal*, Vol. 5, No. 10, 1967, pp. 1760–1767.

[28]Weston, K., and Swanson, J., "A Compilation of Wind Tunnel Heat Transfer Measurements on the Afterbody of the Project Mercury Capsule Reentry Configuration," NASA TM X-495, Aug. 1961.

[29]Hacker, B. C., and Grimwood, J. M., "On the Shoulders of Titans: A History of Project Gemini," NASA SP-4203, 1977.

[30]Raper, R. M., "Heat Transfer and Pressure Measurements Obtained During Launch and Reentry of the First Four Gemini-Titan Missions and Some Comparisons with Wind Tunnel Data," NASA TM X-1407, Aug. 1967.

[31]Malik, P. W., and Souris, G. A., "Project Gemini: A Technical Summary," NASA CR-1106, June 1968.

[32]Huber, P., "Deduction of Reentry Plasma Properties About Manned Orbital Spacecraft from Radio Signal Attenuation Data," NASA TN D-4118, Aug. 1967.

[33]Schroeder, L., and Russo, F., "Flight Investigations and Analysis of Alleviation of Communications Blackout by Water Injection During Gemini 3 Reentry," NASA TM X-1521, Aug. 1967.

[34]Womick, O., "Manned Space Flight Network Performance Analysis for the GT-2 Mission," NASA TM X-55227, May 1965.

[35]Scallion, W. I., and Lewis, J. H., "Flight Parameters and Vehicle Performance for Project Fire Flight I," NASA TN D-2996, Sept. 1965.

[36]Slocumb, T. H., "Project Fire Flight I Heating and Pressure Measurements on the Reentry Vehicle Afterbody at a Velocity of 38,000 Feet Per Second," NASA TM X-1178, Nov. 1965.

[37]Lewis, J. H., and Scallion, W. I., "Flight Parameters and Vehicle Performance for Project Fire Flight II," NASA TN D-3569, Aug. 1966.

[38]Slocumb, T. H., "Project Fire Flight II Afterbody Temperatures and Pressures at 11.35 Kilometers Per Second," NASA TM X-1319, Dec. 1966.

[39]Cauchon, D. L., "Radiative Heating Results from the Fire II Flight Experiment at Reentry Velocity of 11.4 km/s," NASA TM X-1402, July 1967.

[40]Richardson, N. R., "Project Fire Instrumentation for Radiative Heating and Related Measurements," NASA TN D-3646, Oct. 1966.

[41]Woodbury, G., "Angle of Attack Analysis for Project Fire I Reentry Flight," NASA TN D-3366, April 1966.

[42]Scallion, W. I., and Lewis, J. H., "Body Motions and Angles of Attack During Project Fire Flight II Reentry," NASA TN D-4183, Oct. 1967.

[43]Wright, M. J., Loomis, M., and Papadopoulos, P. E., "Aerothermal Analysis of the Project Fire II Afterbody Flow," *Journal of Thermophysics and Heat Transfer*, Vol. 17, No. 2, 2003, pp. 240–249.

[44]Sinha, K., Barnhardt, M., and Candler, G., "Detached Eddy Simulation of Hypersonic Base Flows with Application to Fire II Experiments," AIAA Paper 2004-2633, June 2004.

[45]Crouch, R., and Walberg, G., "An Investigation of Ablation Behavior of Avcoat 5026/39M over a Wide Range of Thermal Environments," NASA TM X-1778, April 1969.

[46]Pavlosky, J. E., and St. Leger, L. G., "Apollo Experience Report: Thermal Protection Subsystem," NASA TN D-7564, Jan. 1974.

[47]Hillje, E., "Entry Flight Aerodynamics from Apollo Mission AS-202," NASA TN D-4185, Oct. 1967.

[48]Hillje, E., "Entry Aerodynamics at Lunar Return Conditions Obtained from the Flight of Apollo 4," NASA TN D-5399, Oct. 1969.

[49]Lee, D., Bertin, J., and Goodrich, W., "Heat Transfer Rate and Pressure Measurements During Apollo Orbital Entries," NASA TN D-6028, Oct. 1970.

[50]Lee, D., "Apollo Experience Report: Aerothermodynamics Evaluation," NASA TN D-6843, June 1972.

[51]Wright, M. J., Prabhu, D. P., and Martinez, E., "Analysis of Apollo Command Module Afterbody Heating, Part 1: AS-202," *Journal of Thermophysics and Heat Transfer*, Vol. 20, No. 1, 2006, pp. 16–30.

[52]Lee, D., and Goodrich, W., "Aerothermodynamic Environment of the Apollo Command Module During Superorbital Entry," NASA TN D-6792, April 1972.

[53]Walton, T. E., Witte, W. G., and O'Hare, B. J., "Flight Investigation of the Effects of Apollo Heat Shield Singularities on Ablator Performance," NASA TN D-4791, Sept. 1968.

[54]Ried, R., Rochelle, W., and Milhoan, J., "Radiative Heating of the Apollo Command Module: Engineering Predictions and Flight Measurement," NASA TM X-58091, April 1972.

[55]Lee, G., "Ablation Effects on the Apollo Afterbody Heat Transfer," *AIAA Journal*, Vol. 7, No. 8, 1969, pp. 1616–1618.

[56]Wright, R., and Zoby, E., "Flight Measurements of Boundary Layer Transition on a 5° Cone at a Mach Number of 20," NASA TM X-2253, May 1971.

[57]Richardson, E., "Re-Entry F Turbulent Heat Experiment Familiarization Manual," NASA CR-66501, Oct. 1967.

[58]Francis, W. L., "Turbulent Base Heating on a Slender Reentry Vehicle," *Journal of Spacecraft and Rockets*, Vol. 9, No. 8, 1972, pp. 620, 621.

[59]Bulmer, B. M., "Flight Test Correlation Technique for Turbulent Base Heat Transfer with Low Ablation," *Journal of Spacecraft and Rockets*, Vol. 10, No. 3, 1973, pp. 222–224.

[60]Dillon, J., and Carter, H., "Analysis of Base Pressure and Base Heating on a 5° Half Angle Cone in Free Flight near Mach 20," NASA TM X-2468, Jan. 1972.

[61]Carter, H., Raper, J., Hinson, W., and Morris, W., "Basic Measurements from a Turbulent Heating Flight Experiment on a 5° Half-Angle Cone at Mach 20 (Reentry F)," NASA TM X-2308, Sept. 1971.

[62]Woodbury, G. E., and Morris, W. D., "Angle-of-Attack Analysis of a Spinning Slender Cone with Slight Aerodynamic and Mass Asymmetries," NASA TN D-5948, Sept. 1970.

[63]Alley, V., and Guillotte, R., "Postflight Analysis of Thermal Distortions of the Reentry F Spacecraft," NASA TM X-2250, May 1971.

[64]Martin-Marietta Corp., "Viking Lander System, Primary Mission Performance Report," NASA CR-145148, April 1977.

[65]Seiff, A., and Kirk, D., "Structure of the Atmosphere of Mars in Summer at Mid-Latitudes," *Journal of Geophysical Research*, Vol. 82, Sept. 1977, pp. 4364–4378.

[66]Martin-Marietta Corp., "Entry Data Analysis for Viking 1 and 2," NASA CR-159388, Nov. 1976.

[67]Schmitt, D., "Base Heating on an Aerobraking Orbital Transfer Vehicle," AIAA Paper 83-0408, Jan. 1983.

[68]Edquist, K. T., Wright, M. J., and Allen, G. A., "Viking Afterbody Heating Computations and Comparison to Flight Data," AIAA Paper 2006-0386, Jan. 2006.

[69]Givens, J., Nolte, L., and Pochettino, L., "Galileo Atmospheric Entry Probe System: Design, Development and Test," AIAA Paper 83-0098, Jan. 1983.

[70]Talley, R. G., "Galileo Probe Deceleration Module Final Report," General Electric Reentry Systems Operations, Rept. 84DS2020, Philadelphia, 1984.

[71]Hughes Space and Communications Co., "Galileo Probe Mission Operations Final Report," Rept. HS373-6000, Los Angeles, Sept. 1996.

[72]Milos, F., Chen, Y.-K., Squire, T., and Brewer, R., "Analysis of Galileo Probe Heat Shield Ablation and Temperature Data," *Journal of Spacecraft and Rockets*, Vol. 36, No. 3, 1999, pp. 298–306.

[73]Nestler, D. E., and Brant, D. N., "Development of an Afterbody Radiative and Convective Heating Code for Outer Planet Probes," AIAA Paper 78-0862, May 1978.

[74]Balakrishnam, A., and Chu, E., "Jupiter Entry Probe Afterbody Convective Heating," AIAA Paper 79-0040, Jan. 1979.

[75]Milos, F. S., "Galileo Probe Ablation Experiment," *Journal of Spacecraft and Rockets*, Vol. 34, No. 6, 1997, pp. 750–713.

[76]Tauber, M. E., Wercinski, P., Yang, L., and Chen, Y.-K., "A Fast Code for Jupiter Atmospheric Entry Analysis," NASA TM-1999-208796, Sept. 1999.

[77]Matsuyama, S., Ohnishi, N., Sasoh, A., and Sawada, K., "Numerical Simulation of Galileo Probe Entry Flowfield with Radiation and Ablation," *Journal of Thermophysics and Heat Transfer*, Vol. 19, No. 1, 2005, pp. 28–35.

[78]Spencer, D., Blanchard, R., Braun, R., Kallemeyn, P., and Thurman, S., "Mars Pathfinder Entry, Descent and Landing Reconstruction," *Journal of Spacecraft and Rockets*, Vol. 36, No. 3, 1999, pp. 357–366.

[79]Willcockson, W. H., "Mars Pathfinder Heatshield Design and Flight Experience," *Journal of Spacecraft and Rockets*, Vol. 36, No. 3, 1999, pp. 374–379.

[80]Milos, F., Chen, Y.-K., Congdon, W., and Thornton, J., "Mars Pathfinder Entry Temperature Data, Aerothermal Heating, and Heatshield Material Response," *Journal of Spacecraft and Rockets*, Vol. 36, No. 3, 1999, pp. 380–391.

[81]Mitcheltree, R., and Gnoffo, P., "Wake Flow About Mars Pathfinder Entry Vehicle," *Journal of Spacecraft and Rockets*, Vol. 32, No. 5, 1995, pp. 771–776.

[82]Haas, B., and Venkatapathy, E., "Mars Pathfinder Computations Including Base Heating Predictions," AIAA Paper 95-2086, June 1995.

[83]Tran, H., Johnson, C., Rasky, D., Hui, F., and Hsu, M., "Silicone Impregnated Reusable Ceramic Ablators for Mars Follow-On Missions," AIAA Paper 96-1819, June 1996.

[84]Schmitt, G., Pfeuffer, H., Kasper, R., Kleppe, F., Burkhardt, J., and Shöttle, U., "The MIRKA Reentry Mission," 49th International Astronautical Congress, IAF-98-V2.07, Sept. 1998.

[85]Jahn, G., Schöttle, U., and Messerschmid, E., "Post-Flight Surface Heat Flux and Temperature Analysis of the MIRKA Reentry Capsule," *Proceedings of the 21st International Symposium on Space Technology*, ISTS, Tokyo, 1998, pp. 532–537.

[86]Fertig, M., and Fruehauf, H., "Detailed Computation of the Aerothermodynamic Loads of the MIRKA Capsule," *3rd European Symposium on Aerothermodynamics for Space Vehicles*, ESA SP-426, 1998, pp. 703–710.

[87]Fruehauf, H., Fertig, M., and Kanne, S., "Validation of the Enhanced URANUS Nonequilibrium Navier–Stokes Code," *Journal of Spacecraft and Rockets*, Vol. 37, No. 2, 2000, pp. 218–223.

[88]Macret, J., and Leveugle, T., "The ARD Program: An Overview," AIAA Paper 99-4934, June 1999.

[89]Paulat, J. C., "Atmospheric Reentry Demonstrator Post Flight Analysis: Aerodynamics," *Proceedings of the 2nd International Symposium on Atmospheric Reentry Vehicles* [CD-ROM], Centre National d'Etudes Spatiales, Paris, Paper 14-052, 2001.

[90]Tran, P., and Soler, J., "Atmospheric Reentry Demonstrator Post Flight Analysis: Aerothermal Environment," *Proceedings of the 2nd International Symposium on Atmospheric Reentry Vehicles* [CD-ROM], Centre National d'Etudes Spatiales, Paris, Paper 14-049, 2001.

[91]Thirkettle, A., Steinkopf, M., and Joseph-Gabriel, E., "The Mission and Post-Flight Analysis of the Atmospheric Reentry Demonstrator," ESA Bulletin 109, Feb. 2002, pp. 56–63.

[92]Véronneau, Y., "Atmospheric Reentry Demonstrator Post Flight Analysis: Surface Pressure," *Proceedings of the 2nd International Symposium on Atmospheric Reentry Vehicles* [CD-ROM], Centre National d'Etudes Spatiales, Paris, Paper 14-048, 2001.

T. Lin
Associate Editor